Journal of Materials Chemistry A

PAPER

View Article Online
View Journal | View Issue

Cite this: J. Mater. Chem. A, 2019, 7, 17854

Highly porous, low band-gap $Ni_xMn_{3-x}O_4$ ($0.55 \leq x \leq 1.2$) spinel nanoparticles with *in situ* coated carbon as advanced cathode materials for zinc-ion batteries†

Jun Long,[ab] Jinxing Gu,[c] Zhanhong Yang,*[a] Jianfeng Mao,[b] Junnan Hao,[b] Zhongfang Chen *[c] and Zaiping Guo *[bd]

Aqueous zinc ion batteries (ZIBs) are emerging as a highly promising alternative technology for grid-scale applications where high safety, environmental-friendliness, and high specific capacities are needed. It remains a significant challenge, however, to develop a cathode with a high rate capability and long-term cycling stability. Here, we demonstrate diffusion-controlled behavior in the intercalation of zinc ions into highly porous, Mn^{4+}-rich, and low-band-gap $Ni_xMn_{3-x}O_4$ nano-particles with a carbon matrix formed *in situ* (with the composite denoted as $Ni_xMn_{3-x}O_4$@C, $x = 1$), which exhibits superior rate capability (139.7 and 98.5 mA h g^{-1} at 50 and 1200 mA g^{-1}, respectively) and outstanding cycling stability (128.8 mA h g^{-1} remaining at 400 mA g^{-1} after 850 cycles). Based on the obtained experimental results and density functional theory (DFT) calculations, cation-site Ni substitution combined with a sufficient doping concentration can decrease the band gap and effectively improve the electronic conductivity in the crystal. Furthermore, the amorphous carbon shell and highly porous Mn^{4+}-rich structure lead to fast electron transport and short Zn^{2+} diffusion paths in a mild aqueous electrolyte. This study provides an example of a technique to optimize cathode materials for high-performance rechargeable ZIBs and design advanced intercalation-type materials for other energy storage devices.

Received 15th May 2019
Accepted 28th June 2019

DOI: 10.1039/c9ta05101e

rsc.li/materials-a

Introduction

Because the escalating population and energy production have been speeding up the combustion of fossil fuels[1] around the world, severe environmental issues are gradually appearing.[2] Therefore, the energy storage market is flourishing in terms of energy-saving technology and technical development.[3,4] Furthermore, it is significant that the obtained energy should be produced from renewable energy resources and be stored[5–7] in effective ways. Environmentally friendly energy storage and conversion based on the electrochemical technology[8–13] can occupy a position of dominance in the energy market,[14] because it can release/store energy with a considerable conversion efficiency.[15–20] Lithium-ion batteries (LIBs) have been widely used in today's society because of their large specific power and high energy density.[21–24] The widespread use of LIBs in power portable electronic devices and grid-scale energy storage could be impractical, however, because they are limited by their high cost[25,26] and flammable electrolyte. Recently reported aqueous metal ion (monovalent-ion, bivalent-ion, multivalent-ion, *etc.*) batteries have garnered much attention owing to their high-energy-density, high-safety, and nontoxicity. Rechargeable aqueous zinc-ion batteries (ZIBs)[27–30] composed of an intercalation/deintercalation cathode, aqueous electrolyte, and zinc metal anode have become one of the most popular research hotspots in the energy and resources sector. Several advantages of ZIBs have already been demonstrated compared to LIBs and other nonaqueous metal ion batteries. First, zinc offers important advantages over lithium due to its natural abundance and low cost, as well as its high theoretical specific capacity (820 mA h g^{-1}) and low working potential (−0.78 V *vs.* the standard hydrogen electrode potential). Second, the processes of zinc deposition and stripping are also facile in an aqueous electrolyte because of its high overpotential. Third, the fewer safety concerns associated with ZIBs could make it possible to scale them up, due to their incombustibility and high

[a]Hunan Provincial Key Laboratory of Chemical Power Sources, College of Chemistry and Chemical Engineering, Central South University, Changsha 410083, P. R. China. E-mail: zhyang@csu.edu.cn

[b]Institute for Superconducting & Electronic Materials, University of Wollongong, Wollongong, New South Wales 2522, Australia. E-mail: zguo@uow.edu.au

[c]Department of Chemistry, Institute for Functional Nanomaterials, University of Puerto Rico Rio, Rio Piedras Campus, San Juan, PR 00931, USA. E-mail: zhongfangchen@gmail.com

[d]School of Mechanical, Materials, Mechatronics and Biomedical Engineering, University of Wollongong, Wollongong, New South Wales 2500, Australia

† Electronic supplementary information (ESI) available. See DOI: 10.1039/c9ta05101e

volumetric capacity (5854 mA h cm^{-3}).[31] Many cathode materials for ZIBs have been reported so far, such as LiV_3O_8,[32] $Na_3V_2(PO_4)_3$,[30] MnO_2,[27] MnS,[33] $ZnMn_2O_4$,[34] $Zn_3V_2O_7(OH)_2\cdot 2H_2O$,[31] Prussian blue,[35] *etc.* Despite these efforts, further scientific research on such excellent cathode materials with a high capacity and remarkable cycling performance is essential, bearing in mind that ZIBs are just in the developmental stage.

Recalling the whole R&D process for Li-insertion cathodes, most previous studies have focused on the AMn_2O_4 (A = Zn, Co, Ni, *etc.*) spinel structure, which can improve the electrochemical performance compared to monovalent alternatives as well as the cycling stability[36,37] because of the multiple Mn valences. Therefore, it is meaningful to explore these structures for Zn-storage. For example, the spinel structure of $ZnMn_2O_4$ (ref. 34) is maintained during the intercalation/de-intercalation process. $Zn(H_2O)_n^{2+}$ (zinc hydrated ions) cannot intercalate into the spinel structure. However, H^+ can insert into the layered structural materials (such as MnO_2 and $NH_4V_4O_{10}$), and OH^- can react with $ZnSO_4$ and H_2O in the electrolyte to produce some large flake-like $ZnSO_4[Zn(OH)_2]_3\cdot xH_2O$.[27,31] Therefore, this phenomenon could increase the pH of the electrolyte. It can be concluded that the structure of the spinel systems is much more stable than the layered materials during cycling. These Mn-based materials have common barriers to wider application, however, such as large volume variation and poor electrical conductivity during the phase transitions in the course of cycling. Among these systems (Mn-based electrodes) researched for energy storage, $NiMn_2O_4$, as one of the most interesting spinel oxides, was widely used in lithium-ion batteries (LIBs) and supercapacitors (SCs) with superior electrochemical activity and structural reversibility[38,39] because of its synergetic Ni–Mn structure. Very recently, cation-site doping has been widely used to enhance its structural stability and intrinsic conductivity. $NiMn_2O_4$ can provide enough redox active sites[40] for critical electrochemical reactions because of the lattice competition between nickel ions and manganese ions in the $NiMn_2O_4$ spinel metal oxide.[41] Furthermore, in contradistinction to other transition metal manganites (AMn_2O_4; A = Mg, Co, Fe, Mn, and Zn), the crystalline structure of the Ni–Mn spinel is a symmetric cubic structure, which shows tetragonal distortion because of the dynamic Jahn–Teller effect[42] related to the existence of trivalent manganese in the octahedral sites. The tetrahedral lattice sites (A-sites) and the octahedral interstices (B-sites) are, respectively, occupied by divalent cations and trivalent cations for a regular spinel.[43–45] Nevertheless, $NiMn_2O_4$ is not the usual type of spinel but a hybrid spinel, where a fraction y of the divalent nickel ions could leave the A-sites and likely be located on the B-sites in the crystal, which is characterized by cubic close packing of oxygen atoms.[42,46–48] This will result in a corresponding $2y$ of the trivalent manganese ions that is disproportional to divalent manganese ions and tetravalent manganese ions in these B-sites, so that, simultaneously, the corresponding divalent manganese ions could migrate to the A-sites to balance the valence change induced by the transfer of divalent nickel ions.[47] This may result in capacity fading during cycling owing to the dissolution of Mn^{2+} for Mn-based materials. A Ni-doped electrode material with Mn^{4+}-rich phases can provide a much more flexible response to the active sites, however, optimizing the cycling stability and suppressing the destruction of the crystal structure.

With these considerations from the above analysis in mind, new highly porous, narrow band-gap, and Mn^{4+}-rich $Ni_xMn_{3-x}O_4$ (x = 0, 0.55, 0.8, 1.0, and 1.2) nano-particles were synthesized in a carbon matrix formed *in situ*. The details are included in the Experimental section in the ESI.† We report highly reversible Zn^{2+} de/intercalation and stable performance for the $Zn/Ni_xMn_{3-x}O_4$@C system for the first time. The unique idea for the design could be principally demonstrated as follows: (I) Ni-doping endows $Ni_xMn_{3-x}O_4$ with a low band-gap, improving its electrical conductivity; (II) Ni-doped Mn^{4+}-rich $Ni_xMn_{3-x}O_4$ can provide much more flexible active sites to preserve the crystal structure; (III) the pores inside $Ni_xMn_{3-x}O_4$ nanoparticles facilitate fast mass/ion transport and penetration in the mild electrolyte; and (IV) $Ni_xMn_{3-x}O_4$ in the $Ni_xMn_{3-x}O_4$@C electrode could anchor the coated carbon strongly and conformally, restraining the aggregation and dissolution of $Ni_xMn_{3-x}O_4$. Based on these synergic effects, the $Zn/Ni_xMn_{3-x}O_4$@C (x = 1) system can work well in an aqueous electrolyte (2 M $ZnSO_4$ + 0.15 M $MnSO_4$), and demonstrate a high specific capacity (133.7 mA h g^{-1} at 200 mA g^{-1}) and long-term cyclability (91.9% capacity retention after 850 cycles at 400 mA g^{-1}) in the range of 1.0–1.85 V. Its electrochemical properties can be improved by controlling the molar ratio of Ni and Mn, owing to the displacement of Ni^{2+} from B sites, which can change the electrical properties introduced by the "hopping mechanism" of Mn^{3+} and Mn^{4+} on the B-sites *via* localized states.[48–50] Moreover, the mechanism of Zn^{2+} de/intercalation in the nonstoichiometric $Ni_xMn_{3-x}O_4$ spinel coated *in situ* with amorphous carbon layers has been deeply studied by *ex situ* X-ray diffraction (XRD), X-ray photoelectron spectroscopy (XPS), scanning electron microscopy (SEM), energy-dispersive spectrometry (EDS), transmission electron microscopy (TEM), first-principles calculations, and nitrogen adsorption/desorption experiments.

Results and discussion

Structural characterization

As shown in Fig. 1a, the synthesis of $Ni_xMn_{3-x}O_4$@C samples with different Ni : Mn ratios was confirmed by powder XRD analysis. The obtained XRD data as a function of the Ni proportion in a series of prepared samples correspond well to the $NiMn_2O_4$ spinel structure (*Fd*3*m*), which indicates that the calcination of precursors did not change the crystal structure of $Ni_xMn_{3-x}O_4$@C. For these $Ni_xMn_{3-x}O_4$@C hybrids, no NiO impurity was detectable except for the $Ni_xMn_{3-x}O_4$@C (x = 1.2) composition, demonstrating the successful transformation of $Ni_xMn_{3-x}O_4$@C (x = 0.55, 0.8, and 1), which was understood by referring to the JCPDS standard. Interestingly, when the Ni content was increased from 0 to 0.55, 0.85 and 1, respectively, $Ni_xMn_{3-x}O_4$@C (x = 0) with the tetragonal Mn_3O_4 (JCPDS, 24-0734, $I4_1/amd$) structure (as shown in Fig. S1 in the ESI†) was gradually transformed into $Ni_xMn_{3-x}O_4$@C (x = 1) with the space group *Fd*3*m*. Compared with $Ni_xMn_{3-x}O_4$@C (x = 0.55,

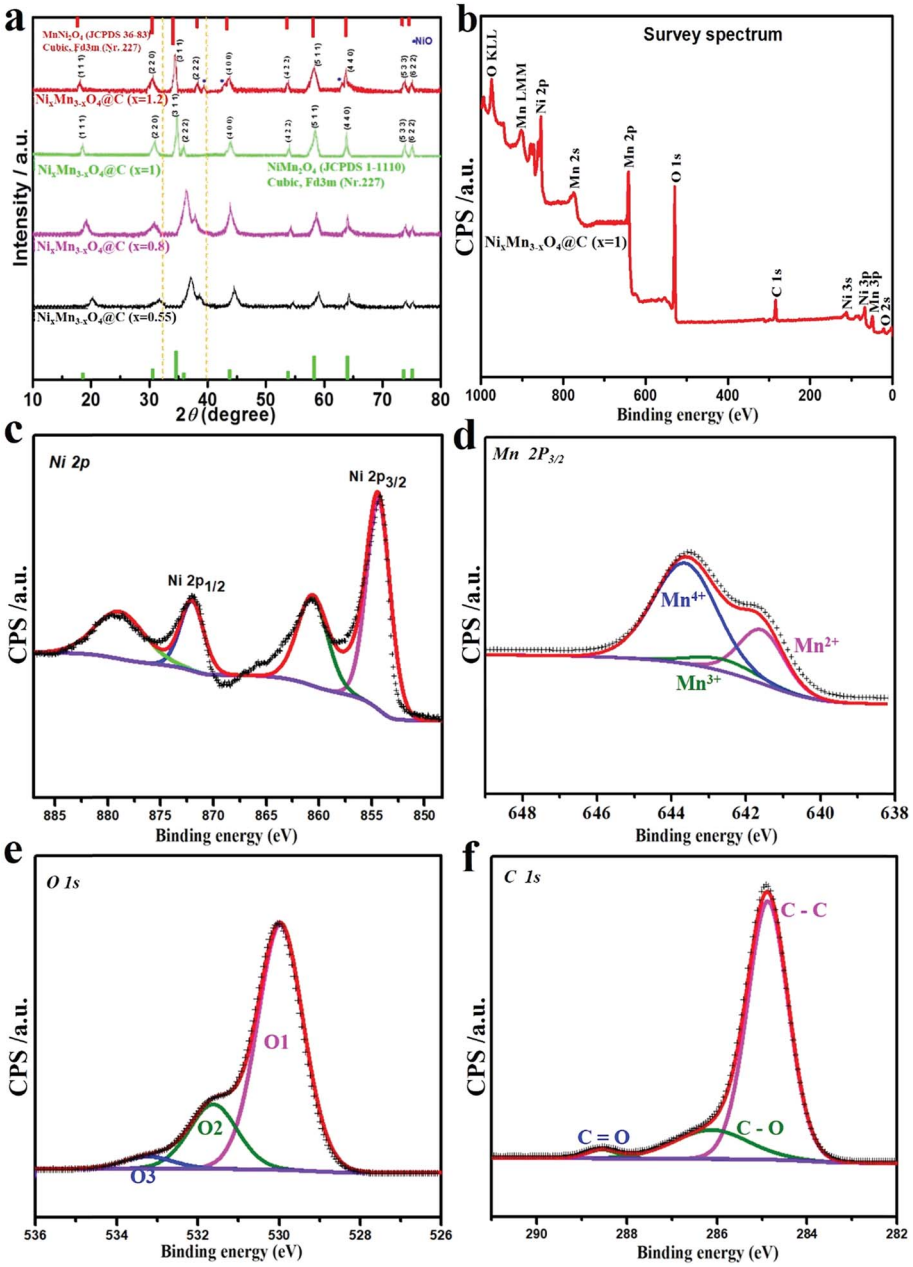

Fig. 1 (a) XRD patterns for $Ni_xMn_{3-x}O_4$@C samples (x = 0.55, 0.8, 1.0, and 1.2). (b) XPS survey spectrum of $Ni_xMn_{3-x}O_4$@C (x = 1). (c–f) XPS narrow scan spectra for Ni 2p (c), Mn $2p_{3/2}$ (d), O 1s (e) and C 1s (f) for $Ni_xMn_{3-x}O_4$@C (x = 1).

0.8), the strong peaks of the $Ni_xMn_{3-x}O_4$@C ($x = 1$) composition at 2θ = 18.3°, 30.15°, 34.95°, 36.86°, 43.52°, 53.54°, 57.90°, 62.95°, 73.99°, and 75.37° correspond to the (111), (220), (311), (222), (400), (442), (511), (440), (533), and (622) reflections in the XRD standard of $NiMn_2O_4$ (JCPDS, 1-1110, *Fd3m*). It has been found, however, that the peaks of NiO (JCPDS, 47-1049, $Fm\bar{3}m$ (225)) were only observed in the $Ni_xMn_{3-x}O_4$@C (x = 1.2) sample, which are labeled with blue stars. This is due to the fact that further increase of the Ni content to 1.2 could lead to the segregation of multiphase materials including NiO and Ni_2MnO_4, which indicates that the substitution limit of Ni for Mn in $Ni_xMn_{3-x}O_4$@C ($x = 1.2$) has been reached. We find that nearly all of the peaks of the samples are shifted to lower 2θ values, especially between the dashed-dotted lines, denoting a larger lattice constant with increasing Ni content. The peaks in Fig. 1a are known to shift to lower 2θ values with the substitution of large radius foreign ions.[51] The ionic radius of Ni^{2+} (69 pm) is larger than that of Mn^{2+} (60 pm), Mn^{3+} (58 pm), and Mn^{4+} (53 pm), consistent with this trend.

To discern the positions of Ni and Mn ions in the lattice interstices, the intensity ratio $R = I_{400}/I_{220}$ can be used to study the distribution between them in AB_2O_4 spinels,[44] and it has been reported that the value of R could change if an increasing proportion of foreign ions is substituted at the A-sites.

Furthermore, the XRD pattern of $Ni_xMn_{3-x}O_4$@C ($x = 0$) was also obtained, as shown in Fig. S1†, as a comparison. In the case of $Ni_xMn_{3-x}O_4$@C ($x = 0$), the obtained R is 1.237. The values of R measured for $Ni_xMn_{3-x}O_4$@C ($x = 0.55$, 0.8, and 1) are 1.228, 1.230 and 1.235, respectively, which indicates that an increasing proportion of Ni^{2+} is likely to be occupying B-sites, substitutes that prefer to occupy Mn-sites instead.[47] This will be further studied by means of density functional theory (DFT). In Fig. S1,† however, all characteristic peaks are indexed to the tetragonal spinel structure of Mn_3O_4 with the space group $I4_1/amd$. In this structure, Mn^{2+} preferentially occupies the A-sites, while Mn^{3+} occupies the B-sites. It is interesting to note that the valence of Mn in Mn_3O_4 may be not the same as that exhibited in $Ni_xMn_{3-x}O_4$@C. The substitution of Ni at the B-sites of Mn_3O_4 could change the valence state of Mn owing to the electroneutrality principle.[47] A similar phenomenon has been reported in a previous study (ref. 52) for substituted $LiM_xMn_{2-x}O_4$ (M = Cr, Li, Ni, *etc.*) spinels.

More importantly, Ni cations in spinels enhanced the cycling capacities[21] of $Li(Ni_yMn_zCo_{1-x-y})O_2$ cathodes for LIBs, and Mn cations stabilized the spinel structure after partial substitution by Ni cations at B-sites. It is noteworthy that cations with a larger ionic radius and lower valence can balance the crystal stress and stabilize the spinel structure if they coexist with other cations with a smaller radius and higher valence state at the B-sites. For example, cooperative synergies between nickel cations (+2) and manganese cations (+4) made it possible to increase the stability[53] of the framework of $LiNi_{1/3}Co_{1/3}Mn_{1/3}$ during charge–discharge cycling.

XPS measurements were carried out to evaluate the oxidation states of Mn and Ni cations in $Ni_xMn_{3-x}O_4$ and $Ni_xMn_{3-x}O_4$@C ($x = 1$), and the corresponding survey spectra are shown in Fig. S2 and 1b.† Fig. 1b demonstrates the existence of signals associated with Ni, Mn, O, and C. The Ni : Mn ratio (1 : 2.002) was also obtained according to the integrated intensity of the corresponding peaks, which was corrected by elemental sensitivity factors. The result from XPS may not be completely dependable, because it is a semi-quantitative method. The obtained Ni/Mn atomic ratio, which is close to the designed value for the experiment, indicates, however, that Ni and Mn cations are homogeneously distributed within the limits of the XPS analytical depth. Ni 2p and Mn $2p_{3/2}$ photoemission spectra are shown in Fig. 1c and d, respectively. In the case of Ni 2p, the spectrum shows the presence of two main peaks at 854.2 eV ($2p_{3/2}$) and 871.9 eV ($2p_{1/2}$) along with two satellite peaks at 860.8 eV and 878.8 eV. Interestingly, the peak distance between the satellites and the main peaks is about 7 eV, whereas the main peak difference is 17.7 eV, similar to the value of 17.6 eV observed for Ni^{2+} (ref. 54) in NiO. The large full width at half maximum (FWHM) for Mn $2p_{3/2}$ signals of $Ni_xMn_{3-x}O_4$@C ($x = 1$) is indicative of multiplet splitting along with the charging effect,[46] owing to the presence of Mn^{4+}, Mn^{3+} and Mn^{2+} ions. The Mn $2p_{3/2}$ spectrum of $Ni_xMn_{3-x}O_4$@C ($x = 1$) composites is a superimposition of Mn^{4+}, Mn^{3+}, and Mn^{2+} peaks, as shown in Fig. 1d, demonstrating that Mn exists in three different oxidation states. These peaks correspond to a binding energy of 643.5 eV, 642.4 eV, and 641.5 eV,[46] respectively. It was observed that the peak area of Mn^{4+} is the largest among them from the results of XPS investigations of the $Ni_xMn_{3-x}O_4$@C ($x = 1$) compound (Table S1, ESI†). Why do we choose it as the example for further studies? $Ni_xMn_{3-x}O_4$@C ($x = 1$) exhibits a fine and stable crystal structure according to the physical characterization, shows a highly Mn^{4+}-rich structure, and displays a good morphology with uniform nanoparticles, as proven below. Furthermore, the as-prepared $Ni_xMn_{3-x}O_4$@C ($x = 1$) has the highest content of Mn^{4+} (as shown in Fig. S3†) in its crystal structure after the precursor is calcined at the target temperature of 455 °C for 2.5 h in an oxygen atmosphere. The O 1s spectrum of $Ni_xMn_{3-x}O_4$@C ($x = 1$) is deconvoluted into three peaks as shown in Fig. 1e, where the peak at 529.9 eV (O1) is due to the metal–oxygen bonds, whereas a weaker peak at 531.5 eV (O2) is correlated with the large amount of –OH species adsorbed on the surface. The smallest peak at 533.2 eV (O3) could be due to chemisorbed oxygen or adsorbed water on the surface of the sample. The core-level C 1s XPS spectrum of $Ni_xMn_{3-x}O_4$@C ($x = 1$) consists of three components centered at 284.8 eV, 286.1 eV and 288.3 eV, corresponding to the C–C, C–O, and C═O bonds, respectively (Fig. 1f).

From these XPS results, the valence of Mn ions could change[46,47] during Ni substitution for Mn in the $Ni_xMn_{3-x}O_4$ structure, which is consistent with the previous discussion. Additionally, Mn^{4+} displays a higher valence than Mn^{3+} but a smaller ionic radius, while Ni^{2+} exhibits a lower valence than Mn^{3+} but a larger ionic radius. The substitution of Ni species[9] in the crystal structure has been proven to boost the reversible capacity, while Mn species ameliorate the interfacial impedance[1] and enhance the electrochemical performance. Therefore, the synergies of Mn^{4+}–Ni^{2+} and their substitution at the B-sites balance the valence charge in the crystal lattices, which relieves the crystal stress owing to the mismatching ionic radius and hence promotes the stability of the spinel structure. Furthermore, the Mn^{4+} rich phase in $Ni_xMn_{3-x}O_4$@C ($x = 1$) can act as protective component to improve the medium to promote zinc ion diffusion and alleviate Mn^{2+} dissolution during charge–discharge. According to the above-mentioned research results, it has been observed that the intensive synergic action between Ni^{2+} and Mn^{4+} at B-sites could be used as the evidence for the reversibility and stability of the active materials during charge/discharge. Furthermore, more details on the changes to the microstructure and the lattice defects of the obtained samples were also revealed by Raman spectroscopy (Fig. S4†) and Fourier transform infrared (FTIR) spectroscopy (in Fig. S5†), which are complementary and provide valuable information on the chemical bonds in Ni–Mn–O systems in the hybrids.

It can be seen from the Raman spectra (in Fig. S4†) of $Ni_xMn_{3-x}O_4$@C hybrids that the intense vibrational modes located around 654 cm^{-1} and 556 cm^{-1} are assigned as the A_{1g} and F_{2g} modes, respectively. The peak located at 556 cm^{-1} reflects the symmetric Ni–O stretching vibration derived from the F_{2g} mode[55] in $NiMn_2O_4$. The A_{1g} active mode originates from the symmetric Mn^{4+}–O (MnO_6) stretching vibration at octahedral sites.[56] Interestingly, the Mn^{2+}–O and Mn^{4+}–O vibrations at A-sites and B-sites are in accordance with the results obtained from the above XRD and XPS analysis. Additionally, the T_{2g}

(located at 305 cm^{-1}) and E_g (located at 372 cm^{-1}) modes gradually disappear as x increases in the $Ni_xMn_{3-x}O_4$@C compounds, and the F_{2g} and Ni–O (locates at 509 cm^{-1}) stretching modes appear. These results indicate that Mn^{3+}–O is transformed into Mn^{4+}–O at the B-sites during Ni substitution for Mn in the $Ni_xMn_{3-x}O_4$ structure. Typical carbon peaks located at 1362 cm^{-1} (D band) and 1580 cm^{-1} (G band) are detected from the samples. Furthermore, Fourier transform infrared (FTIR) spectroscopy is a complementary characterization method, which provides valuable information of Ni–Mn–O systems. The absorption peaks at 597 cm^{-1} and 507 cm^{-1} are assigned to Mn–O_4 and Mn–O_6 (ref. 56) vibrations (Fig. S5†), respectively, and the lower absorption bands at 452 cm^{-1} can be assigned to Ni–O_6, indicating that Ni can substitute Mn at the B-sites along with the change in the valence of Mn^{3+} at the B-sites. It should be noted that Mn^{4+} and Ni^{2+} at the B-sites take the place of Mn^{3+} in the compounds, as evidenced by XRD, XPS, Raman spectroscopy, and FTIR spectroscopy analyses.

The overall typical nanoparticle morphologies of the as-prepared $Ni_xMn_{3-x}O_4$@C compounds and their crystal phases were characterized by using SEM, selected-area electron diffraction (SAED) analysis, energy dispersive X-ray spectroscopy (EDX) elemental mapping, and high resolution TEM (HRTEM) (as shown in Fig. 2 and S6†). The samples show an irregular particle morphology with a size range of 15–25 nm (Fig. 2a–c), and the morphology is transformed into more

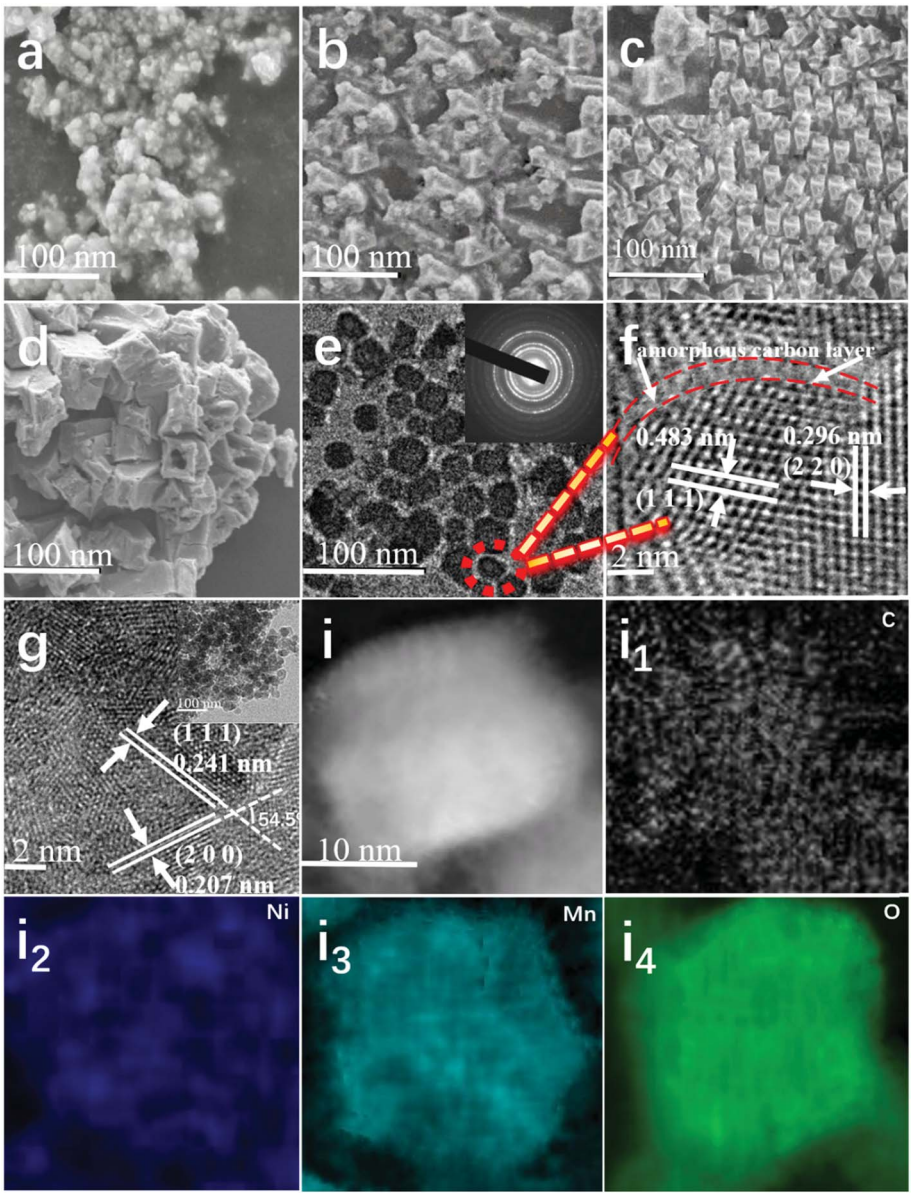

Fig. 2 (a–d) SEM images of $Ni_xMn_{3-x}O_4$@C samples: $x = 0.55$ (a), $x = 0.8$ (b), $x = 1$ (c), and $x = 1.2$ (d). (e) TEM image of $Ni_xMn_{3-x}O_4$@C ($x = 1$); inset: the corresponding SAED pattern. (f) HR-TEM image of the indicated area in (e). (g) HR-TEM image of $Ni_xMn_{3-x}O_4$@C ($x = 1$), with the inset showing the corresponding low-resolution TEM image. (i) Scanning TEM (STEM) image of a $Ni_xMn_{3-x}O_4$@C ($x = 1$) nanoparticle, with (i_1–i_4) showing the corresponding EDX elemental maps of C (i_1), Ni (i_2), Mn (i_3), and O (i_4).

irregular aggregated rectangular bulks (Fig. 2d) on a large scale ($x = 1.20$), indicating that an insufficient or excess content of Ni in the $Ni_xMn_{3-x}O_4$@C compounds can affect the morphology of the nanoparticles. Therefore, high-resolution TEM and low-resolution TEM images (Fig. 2g and its inset) of $Ni_xMn_{3-x}O_4$@C ($x = 1.2$) reveal various aggregates with mixed phases. The lattice spacings measured in Fig. 2g shows interplanar spacings of 0.241 nm and 0.207 nm corresponding to the (1 1 1) and (2 0 0) planes of crystalline NiO, which are consistent with the XRD (Fig. 1) and SAED (Fig. S6b†) results. Furthermore, the EDX spectrum (Fig. S6a†) demonstrates that the ratio of Ni : Mn is 1 : 2.026 in $Ni_xMn_{3-x}O_4$@C ($x = 1$), whereas the ratio of Ni : Mn is 1 : 2.002 according to inductively coupled plasma-atomic emission spectrometry (ICP-AES) results. The differences between these two values and the theoretical ratio are quite small, further demonstrating the successful substitution of Mn by Ni. Elemental mapping images (Fig. 2i–i_4) of C, Ni, Mn, and O manifest no distinct phase segregation, revealing a homogeneous distribution of Ni and Mn elements in the $Ni_xMn_{3-x}O_4$@C ($x = 1$) hybrid. The diffraction rings obtained from the SAED (inset of Fig. 2e) characterization indicate the polycrystalline nature of this sample. The HRTEM lattice image of this compound is also shown in Fig. 2f, which displays well-defined crystalline planes with *d*-spacings of 0.483 nm and 0.296 nm, corresponding to the (1 1 1) and (2 2 0) lattice planes of the face-centred cubic spinel (*Fd3m*) phase, respectively. As seen in Fig. 2e and f, there is a thin amorphous carbon layer (~2 nm) coated on the surface of $Ni_xMn_{3-x}O_4$@C ($x = 1$), which can be conducive to restraining the aggregation and volume changes of $Ni_xMn_{3-x}O_4$@C ($x = 1$) nanocrystals during charge/discharge and improving the conductivity of the electrode. The weight percentage of carbon (9.8 wt%) was determined by thermogravimetric (TG) analysis, as shown in Fig. S7.† Additionally, the mesoporous structure of the $Ni_xMn_{3-x}O_4$@C ($x = 1$) compound is confirmed by an obvious hysteresis loop (Fig. S6c†) in the N_2 adsorption–desorption isotherms, proving a large surface area of 75.275 $m^2\ g^{-1}$ and a wide pore-size distribution at ~4.76 nm (the pore volume is calculated to be ~0.39 $cm^3\ g^{-1}$).

Electrochemical performance

We investigated the electrochemical properties of the $Ni_xMn_{3-x}O_4$@C samples using typical coin cells, employing a Zn foil anode, glass fiber separator, and aqueous electrolyte (2 M $ZnSO_4$ + 0.15 M $MnSO_4$), and a schematic illustration of the ZIB is presented in Fig. 3a. Enlarged views of the cathode and the interior of $Ni_xMn_{3-x}O_4$@C ($x = 1$) are shown in Fig. 3b and c, respectively. $Ni_xMn_{3-x}O_4$ inside the nano-particles generates numerous narrow pores so that zinc ions could transfer more efficiently through these tunnels (Fig. 3d). The uniquely designed $Ni_xMn_{3-x}O_4$@C ($x = 1$) with its spinel structure and conductive carbon network provides superior electrochemical performance. Fig. 3e displays the possible reaction mechanism of zinc ion intercalation/deintercalation in $Ni_xMn_{3-x}O_4$@C ($x = 1$). Fig. 4a shows the cyclic voltammetry (CV) curves of $Ni_xMn_{3-x}O_4$@C ($x = 1$) measured between 1.0 and 1.85 V within the first eleven cycles at a scan rate of 0.3 mV s^{-1}. The profiles in the first and third cycles are slightly shifted to higher potentials in comparison with the following cycles, which can be related to the initial activation of the electrode. During cycling, the polarization of the electrode decreases from the third cycle, as demonstrated (in Fig. S8†) by electrochemical impedance spectroscopy (EIS) analysis. The CV curves (Fig. 4a) prove that there is only one pair of redox peaks for $Ni_xMn_{3-x}O_4$@C ($x = 1$) at about 1.34/1.52 V during subsequent cycles, which can be attributed to Zn^{2+} deintercalation/intercalation from/into the host, consistent with the voltage plateaus shown in the charge and discharge curves (Fig. 4b). The first discharge plateau at about 1.30 V corresponds to Zn^{2+} intercalation into the cathode, while the first charge plateau at about 1.55 V originates from Zn^{2+} extraction. The pair of redox peaks of $Ni_xMn_{3-x}O_4$@C ($x = 1$) at 1.34/1.52 V could be attributed to the reversible conversion of Mn^{3+}/Mn^{4+}, which can be attributed to the corresponding phase transition during charge/discharge. The charge storage kinetics and phase transition in the $Ni_xMn_{3-x}O_4$@C ($x = 1$) host will be discussed below.

As expected, the possible cathodic process may proceed as follows:

$$Ni_xMn_{3-x}O_4 + yZn^{2+} + 2ye^- \leftrightarrow Zn_yNi_xMn_{3-x}O_4 \quad (1)$$

Furthermore, the CV data indicate little change in the potential or peak area loss after the third cycle for all the redox features, proving that $Ni_xMn_{3-x}O_4$@C ($x = 1$) can be an appropriate cathode candidate for aqueous ZIBs.

Fig. 4b presents the discharge/charge curves of the $Ni_xMn_{3-x}O_4$@C ($x = 1$) electrode cycled at a current density of 150 mA g^{-1} within the voltage window of 1.0–1.85 V. The active material delivers initial specific discharge and charge capacities of 115 mA h g^{-1} and 119 mA h g^{-1}, respectively. After 100 cycles, the electrode sustains a stable capacity of around 130 mA h g^{-1} with a high coulombic efficiency (CE) of around 100%. The average discharge plateau is 1.37 V during cycling, giving an excellent energy density of ~178.1 W h kg^{-1} according to the active mass. The $Ni_xMn_{3-x}O_4$@C ($x = 1$) nanoparticles can provide a calculated energy density of 67 W h kg^{-1} under the condition that the content of cathode materials accounts for one third of the whole weight of the battery, which is much higher than that for Ni–Cd (about 50 W h kg^{-1}) and Pb–acid (about 30 W h kg^{-1}) batteries. In comparison, a $Ni_xMn_{3-x}O_4$ + C ($x = 1$) mixture (9.8 wt% carbon) displays an obviously lower capacity of 44 mA h g^{-1} at 100 m A g^{-1} after 100 cycles (Fig. S9†). To evaluate the capacity from the carbon layer coated *in situ* on the surface of $Ni_xMn_{3-x}O_4$@C ($x = 1$), galvanostatic charge/discharge curves (Fig. S10†) of the carbon matrix synthesized by the same method were collected between 1.0 and 1.85 V at 15 mA g^{-1} and indicate that the obtained capacity (~0.5 mA h g^{-1}) can be neglected. Fig. 4d presents the cycling performance of the obtained samples at 250 mA g^{-1} over 400 cycles. All the samples clearly display a gradual capacity increase before 53 cycles owing to the process of electrochemical activation. The capacity of $Ni_xMn_{3-x}O_4$@C ($x = 0$ and 0.55) began to drop quickly after electrochemical activation,

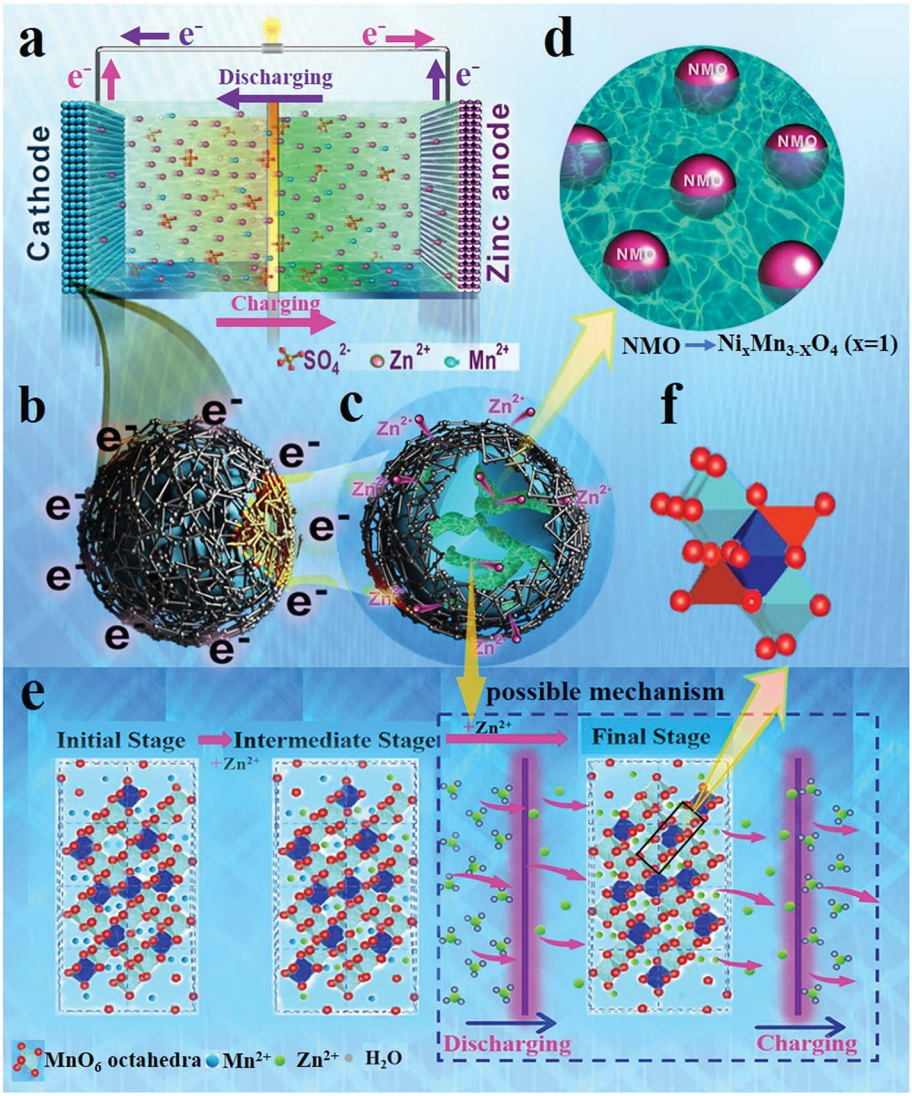

Fig. 3 (a and b) Schematic illustration of a ZIB comprising the $Ni_xMn_{3-x}O_4$@C ($x = 1$) cathode, a battery separator and a zinc anode, as well as a partially enlarged area of the cathode material. (c and d) Enlarged view of the interior of $Ni_xMn_{3-x}O_4$@C ($x = 1$) particles, with $Ni_xMn_{3-x}O_4$ inside the nano-particles generating numerous tunnels so that Zn^{2+} could transfer more efficiently through these tunnels. (e) Schematic illustration of the reaction pathways of zinc ion intercalation/deintercalation into/from the $Ni_xMn_{3-x}O_4$@C ($x = 1$) electrode. (f) Basic unit of the $Ni_xMn_{3-x}O_4$ spinel structure.

however, and its capacity retention ratios are 45% and 48% after 400 cycles, respectively, representing bad electrochemical performance. The $Ni_xMn_{3-x}O_4$@C ($x = 1$, 1.2) composites present better cycling stability than other samples owing to the sufficient substitution of Ni, which also can affect the crystalline structure of $Ni_xMn_{3-x}O_4$, as discussed in Section of structure characterization. The discharge capacity of $Ni_xMn_{3-x}O_4$@C ($x = 1$) is the highest (130 mA h g^{-1} after 400 cycles) among them with a shortened activation process, indicating enhanced Zn^{2+} deintercalation/intercalation kinetics. This excellent cycling performance could be principally due to several factors. First, the characteristic inverse spinel structure with abundant pores and Mn^{4+}-rich crystalline phases could provide countless bonding sites and shorten the Zn^{2+} ion diffusion paths. Second, the moderate amounts of Mn^{2+} in the electrolyte efficiently suppress the structural collapse of $Ni_xMn_{3-x}O_4$, which can enhance the cycling stability and reduce the deterioration of the electrochemical performance (as shown in Fig. S11†). Third, the homogeneous *in situ* carbon coating can enhance the ionic and electronic conductivities and increase cycling stability. The impressive zinc ion storage performance of $Ni_xMn_{3-x}O_4$@C ($x = 1$) is further emphasized by its excellent rate capability. Fig. 4e presents the rate performance at different current densities, and the corresponding cycle profiles are shown in Fig. 4c. The cell displays a reversible discharge capacity of 130 mA h g^{-1} at a current density of 400 mA g^{-1}, which is close to the achieved discharge capacity (139 mA h g^{-1}) at a lower current density of 50 mA g^{-1}. It should be noted that the obtained capacities from 50 mA g^{-1} to 100 mA g^{-1} are nearly invariable. This similarity in capacity demonstrate that 139.7 mA h g^{-1} is the limit for the

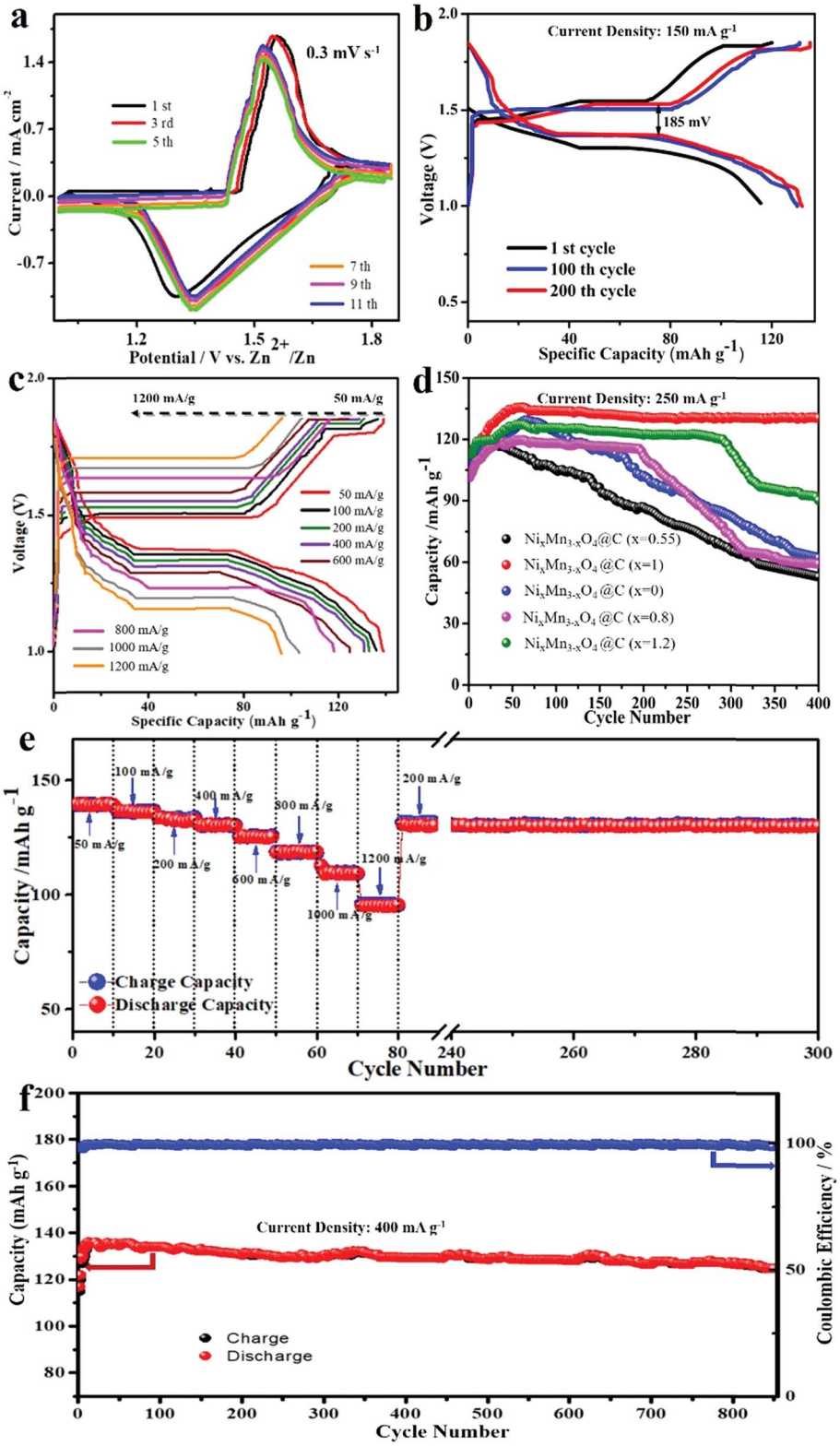

Fig. 4 (a) CV curves of $Ni_xMn_{3-x}O_4$@C ($x = 1$) measured within the first eleven cycles at a scan rate of 0.3 mV s^{-1}. (b) Charge–discharge voltage curves for selected cycles of the electrode at 150 mA g^{-1}. (c) Charge–discharge profiles of $Ni_xMn_{3-x}O_4$@C ($x = 1$) at different rates. (d) Cycling performance of $Ni_xMn_{3-x}O_4$@C ($x = 0$, 0.55, 0.8, 1, and 1.2) samples at 250 mA g^{-1}. (e) Rate capability of the $Ni_xMn_{3-x}O_4$@C ($x = 1$) electrode and its cycling performance after rate tests at 200 mA g^{-1}. (f) Cycling performance and coulombic efficiency of $Ni_xMn_{3-x}O_4$@C ($x = 1$) at 400 mA g^{-1} over 850 cycles.

deintercalation/intercalation of zinc ions from/into the Ni_x-$Mn_{3-x}O_4$@C ($x = 1$) hybrids. As the current density increases to 600 mA g^{-1}, 800 mA g^{-1}, 1000 mA g^{-1}, and 1200 mA g^{-1}, the reversible capacity progressively decreases to 90%, 85%, 79%, and 68%, respectively. The capacity fading (in Fig. 4e) is not irreversible when the cell is cycled at 1200 mA g^{-1}, because it can recover the previous capacity when subsequently cycled at a current density of 200 mA g^{-1}. The rate performance of Ni_x-$Mn_{3-x}O_4$@C ($x = 1$) is superior to that of the other samples, as confirmed in Fig. S12.† Moreover, the $Ni_xMn_{3-x}O_4$@C ($x = 1$) electrode could operate for more than 200 cycles with a high reversible capacity (nearly ~97% recovery of the capacity) of 131 mA h g^{-1} after the rate test. The long cycling stability of $Ni_xMn_{3-x}O_4$@C ($x = 1$) was further investigated at 400 mA g^{-1} over 850 cycles. As can be seen in Fig. 4f, the reversible capacity is 129.5 mA h g^{-1} after dozens of cycles of activation and remains stable in the subsequent cycles, demonstrating superior cycling stability. Furthermore, the coulombic efficiency was increased significantly to 97.8% after about 35 cycles, and then it reaches almost 100% subsequently. The typical plateaus and shapes of the discharge/charge profiles of $Ni_xMn_{3-x}O_4$@C ($x = 1$) at 400 mA g^{-1} were also recorded after different cycles (Fig. S13†), further manifesting its superb cycling stability. Compared with the reported cathode materials (in Table S2†) and other Mn-based materials (in Fig. S14†), it shows remarkable cycling stability.

Zn intercalation mechanism

Structural studies and electrochemical investigations were used to further understand the deintercalation/intercalation mechanism and storage behavior of the $Ni_xMn_{3-x}O_4$@C electrodes. *Ex situ* XPS (Fig. S15a and b†) and XRD measurements (Fig. 5a and b) were carried out to analyze the mechanism of zinc ions deintercalation/intercalation from/into the $Ni_xMn_{3-x}O_4$@C ($x = 1$) host. The *ex situ* XRD study was conducted in the range from 15° to 77° during the first cycle in ZIBs. All the peaks could be indexed to the $Ni_xMn_{3-x}O_4$ structure for the pristine electrode. The (1 1 1), (2 2 0), (5 1 1), and (4 4 0) peaks in the patterns display an obvious shift to lower 2θ angles during discharge and return to their original positions in the following charge, which can be attributed to more zinc ions being extracted/inserted within the tested voltage range. Furthermore, some additional peaks, except for those of the current collector, emerge in the subsequent deintercalation/intercalation, in the potential region where the $Ni_xMn_{3-x}O_4$@C ($x = 1$) host was intercalated by plenty of zinc ions. During the first discharge platform above 1.35 V, only two sets of peaks exist, which are related to pristine $Ni_xMn_{3-x}O_4$@C ($x = 1$) and the steel current collector. Subsequently, some new peaks rose gradually and the peaks of Ni_x-$Mn_{3-x}O_4$@C ($x = 1$) decreased during the following discharge process. The new peaks began to diminish and disappear little by little, while the peaks of $Ni_xMn_{3-x}O_4$@C ($x = 1$) recovered to the original pattern during the subsequent charge process, demonstrating the excellent structural stability of the Ni_x-$Mn_{3-x}O_4$@C ($x = 1$) nano-composite. We note that a small amount of Mn ions shifted to the A-sites from the B-sites, leading to some Mn-associated vacancies, which may induce some zinc ion diffusion along with the consequent structural transformation in the voltage range of about 1.4–1.0 V during discharge/charge. The crystal structure of the active materials can be preserved, however, because of the synergetic effects of Mn^{2+} and Zn^{2+} in the electrolyte, indicating the significantly reversible behavior of $Ni_xMn_{3-x}O_4$@C ($x = 1$). Good reversibility of zinc stripping/plating (Fig. S16a and b†) can be observed for the Zn^{2+} electrolyte with the Mn^{2+} additive, which showed a decrease of the overpotential during cycling. In addition, the peak positions for the intermediate transition phase (rich in zinc ions) can be indexed to the nickel zinc manganite spinel structure, $(Zn_{0.988}$-$Mn_{0.012})(Mn_{1.326}Zn_{0.024}Ni_{0.65})O_4$ (JCPDS no. 04-01-070-6709). As shown in Fig. S15b,† the intensity of Zn_{2p} in the discharge states is far above that in the charge states, further manifesting the intercalation/deintercalation of zinc ions into/from the Mn^{4+}-rich host. The zinc signal in Fig. S15b† did not disappear completely, which can be attributed to the residual Zn^{2+} (on the surface of the host) from the electrolyte. Moreover, the CV curves at various scan rates after activation at a scan rate of 0.2 mV s^{-1} for three cycles are presented in Fig. 5c. Obviously, the peaks gradually grow broad and high with increasing scan rate, but the shapes of the obtained CV curves remain consistent. As assumed, only one pair of redox peaks could be detected at a scan rate from 0.4 to 1.8 mV s^{-1} within the range of 1.0–1.85 V for each CV curve, which ought to be attributed to the Mn^{4+}/Mn^{3+} redox couple reactions, together with step by step Zn^{2+} insertion/extraction into/from the tetrahedral sites of the $Ni_xMn_{3-x}O_4$@C ($x = 1$) framework. XPS spectra of the O 1s and Mn 3s orbitals for $Ni_xMn_{3-x}O_4$@C ($x = 1$) were recorded after discharge/charge. As can be seen from Fig. S17a,† the O 1s XPS spectra for $Ni_xMn_{3-x}O_4$@C ($x = 1$) are different between the charge state and the discharge state, while the positive shift of the stronger peak at 530.1 eV can be attributed to the intercalation of Zn^{2+} into the sample during discharge. The Mn 3s spectra (Fig. S17b†) contain two peaks, which are separated by 5.2 eV after discharge,[57] indicating the reduction of Mn^{4+} to Mn^{3+}. The Mn 3s spectra also contain two peaks that are separated by 4.7 eV after charge, which reflects Mn^{3+} to Mn^{4+} conversion (ref. 58) and the extraction of Zn^{2+} from the sample. Therefore, it is reasonable to assume that the spinel host can support a zinc-rich and zinc-depleted state without obvious polarization during the electrochemical processes for the electrode between 1.0 and 1.85 V, indicating good reversibility and excellent cycling stability. To obtain further insight into the zinc-storage mechanisms of the electrode, kinetic analysis according to the scan rate of CV curves was carried out to research the contributions to the capacity of the diffusion-controlled and capacitive controlled processes. The relationships between the scan rate (v) and the measured peak current (i) are shown in Fig. 5d, which can be depicted as in the following equation:

$$i = av^b \quad (2)$$

where a and b are adjustable parameters, and the b-values can be obtained from the calculation of the slope of the plot ($\log i$ *versus* $\log v$), which can be described as follows:

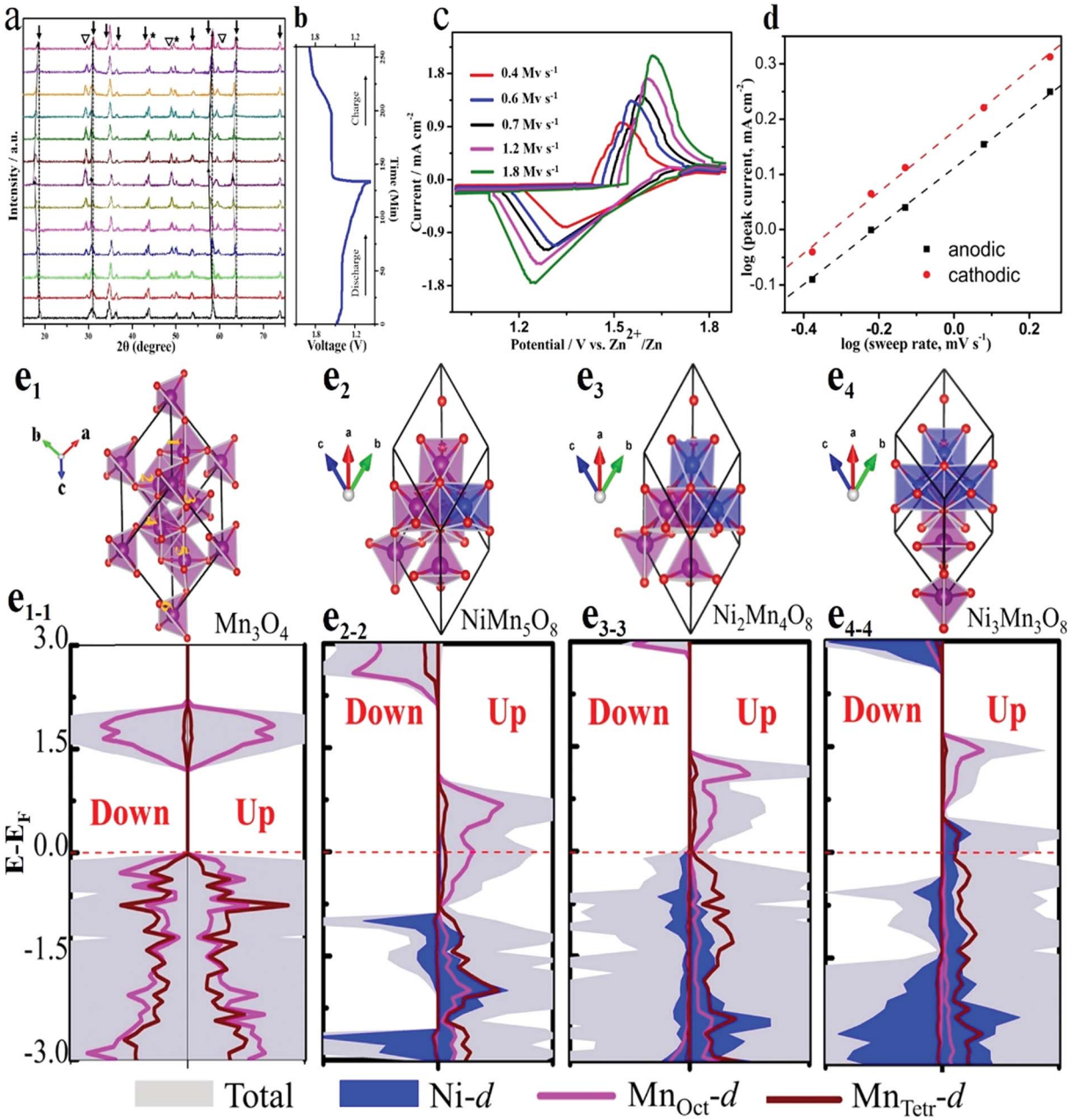

Fig. 5 (a) *Ex situ* XRD patterns of the $Ni_xMn_{3-x}O_4$@C ($x = 1$) cathode for zinc ion batteries during discharging/charging; * stainless steel current collector, ↓ $Ni_xMn_{3-x}O_4$@C ($x = 1$), $(Zn_{0.988}Mn_{0.012})(Mn_{1.326}Zn_{0.024}Ni_{0.65})O_4$. (b) Corresponding voltage–time curves. (c) CVs collected at various scan rates. (d) Log *i vs.* log *v* plots at specific peak currents. (e_1–e_4) Structures of pure Mn_3O_4 and $Ni_xMn_{3-x}O_4$: (e_1–e_4) primitive cells of (e_1) Mn_3O_4 with the space group $I4_1/amd$, (e_2) $NiMn_5O_8$, (e_3) $Ni_2Mn_4O_8$, and (e_4) $Ni_3Mn_3O_8$ based on the primitive cell of Mn_3O_4 by replacing octahedrally coordinated Mn atoms. (e_{1-1}–e_{4-4}) Partial density of states (PDOS) of pure Mn_3O_4 (e_{1-1}), $NiMn_5O_8$ (e_{2-2}), $Ni_2Mn_4O_8$ (e_{3-3}), and $Ni_3Mn_3O_8$ (e_{4-4}); the grey area shows the total DOS, and the other colours indicate the d orbitals of the transition metals.

$$\log i = \log a + b \log v \quad (3)$$

In particular, the *b*-value can vary between 0.5 and 1.0 under well-defined conditions. A *b*-value of 0.5 demonstrates a completely diffusion-dominated intercalation behavior, while a *b*-value of 1.0 indicates a typical capacitive process. The *b*-values of 0.53 for anodic peaks and 0.55 for cathodic peaks can be matched at a scan rate from 0.4 to 1.8 mV s^{-1}, manifesting the kinetics of a diffusion-controlled process. In addition, the charge-transfer resistance (~109 Ω) of $Ni_xMn_{3-x}O_4$@C ($x = 1$) is somewhat lower than for the other samples after 100 cycles at 250 mA g^{-1}, as shown in Fig. S18,† indicating higher electrical conductivity. CV measurements using a three-electrode system were conducted. Notably, the aqueous electrolyte (2 M $ZnSO_4$ + 0.15 M $MnSO_4$) supports a wide electrochemical window as shown in Fig. S19,† and O_2 evolution was suppressed significantly up to 2.15 V.

In order to further prove the relationship between electrical conductivity and the amount of Ni substitution in the B-sites, the projected density of states (PDOS) of $Ni_xMn_{3-x}O_4$ was calculated. Clearly, Fig. $5e_{1-4}$ displays the unit cells of pure Mn_3O_4 and other $Ni_xMn_{3-x}O_4$ materials, where pure Mn_3O_4 has a spinel structure, which belongs to the $I4_1/amd$ space group because of the Jahn–Teller distortion effect, while according to our experiments, Ni doped Mn_3O_4 has the space group $Fd\bar{3}m$. To simulate $Ni_xMn_{3-x}O_4$ with various Ni concentrations, we chose the $Fd3m$ unit cell containing six Mn atoms. Various values of x (0.55, 0.80, 1.00, and 1.20) in $Ni_xMn_{3-x}O_4$ correspond to the chemical formulas $Ni_{1.1}Mn_{4.9}O_8$, $Ni_{1.6}Mn_{4.4}O_8$, $Ni_2Mn_4O_8$, and $Ni_{2.4}Mn_{3.6}O_8$, respectively. Very large supercells are required to make the numbers in these chemical formulas integers, which is computationally demanding and complicated. Therefore, three tuned chemical formulas were selected for simplification, which are $NiMn_5O_8$ ($x = 0.5$), $Ni_2Mn_4O_8$ ($x = 1.0$), and $Ni_3Mn_3O_8$ ($x = 1.5$). Note that all the Ni atoms occupy the B-sites. Therefore, the preference of Ni^{2+} for B-sites is also proven by our computational results, where the B-site occupation in $Ni_xMn_{3-x}O_4$ is energetically more favorable (Fig. S20†), which is similar to the results of our previous XRD analysis. The DOS demonstrates that pure Mn_3O_4 is a semiconductor and that its band gap is about 1.20 eV (in Fig. $5e_{1-1}$). Besides the metallic conductivity, $NiMn_5O_8$ ($x = 0.5$) and $Ni_2Mn_4O_8$ ($x = 1.5$) are so-called half-metals, meaning that only spin up electrons are conductive, as shown in Fig. $5e_{2-2}$ and e_{4-4}. Whereas $Ni_2Mn_4O_8$ ($x = 1.0$) differs slightly around the Fermi level, with the Fermi level crossing the spin-up and spin-down bands (in Fig. $5e_{3-3}$), which suggests that ferrimagnetism ($x = 1$) with a similar x value (around 1.0) could make this sample more conductive than the other samples.

Experimental section

Synthesis of porous $Ni_xMn_{3-x}O_4$@C ($0.55 \leq x \leq 1.2$) nanoparticles

In a typical synthesis, a mixture of $Ni(Ac)\cdot 4H_2O$ and $Mn(Ac)\cdot 4H_2O$ was dissolved in 95 mL of distilled water. The mixture was incubated in a water-bath at a constant temperature of 45 °C, and after magnetic stirring for 90 min, a light blue transparent liquid was obtained. Meanwhile, citric acid (CA) (0.25 M, 95 mL) was then added to the above mixed solution dropwise, which was generally controlled at about one drop per second. After 2 hours, the temperature was increased from 45 °C to 85 °C. Next, the temperature was maintained, and the mixture was stirred overnight until all the water in the container was evaporated. The wet sample was washed and filtered with acetone and ethanol. Then it was dried by using a supercritical dryer, which started at 15 °C, with the temperature subsequently increased to 38 °C while flowing CO_2 was injected into the autoclave (corresponding pressure of about 20 MPa and lasting for 5 h). The as-synthesized sample was ground and further annealed with a heating rate of 8 °C min^{-1} up to the target temperature of 455 °C, which was maintained for 2.5 h in an oxygen atmosphere in a tube furnace. Finally, a calcination procedure is performed with a given heating rate of 5 °C min^{-1} up to the target temperature of 650 °C, which was maintained for 9 h in a tube furnace under an Ar atmosphere with a flow of 80 sccm. In order to change the proportion of nickel (x) in the obtained nanoparticles, different Ni : Mn ratios were designed, yielding porous spinel nanoparticles ($Ni_xMn_{3-x}O_4$@C) with $x = 0.55$, 0.80, 1.00, and 1.20.

For comparison, $Ni_xMn_{3-x}O_4$@C ($x = 0$) was obtained by a similar method to $Ni_xMn_{3-x}O_4$@C ($x = 1$). In order to research whether Mn^{4+}-rich $Ni_xMn_{3-x}O_4$@C exists in the compounds, $Ni_xMn_{3-x}O_4$@C ($x = 1$) was selected as the study subject (the reason is given in the text). The precursor of $Ni_xMn_{3-x}O_4$@C ($x = 1$) was annealed with a heating rate of 8 °C min^{-1} at target temperatures of 365, 410, and 500 °C, which were maintained for 2.5 h in an oxygen atmosphere in a tube furnace, and the ongoing processes are the same as in the above operations. All of the related chemical reagents are of analytical pure grade and used as received without further purification for all the experiments. Inductively coupled plasma-atomic emission spectroscopy (ICP-AES) was used to confirm the contents of Mn and Ni in the as-prepared samples.

Conclusion

In conclusion, highly porous Mn^{4+}-rich $Ni_xMn_{3-x}O_4$@C ($x = 1$) nano-particles wrapped with an *in situ* formed carbon matrix have been successfully fabricated by a facile and eco-friendly method, and the composite has been evaluated as a cathode material for an aqueous rechargeable ZIB. In this resulting composite, the substitution of Mn by Ni at the B-sites of Mn_3O_4 was studied by ICP-AES, XPS, XRD, and DFT calculations, which demonstrate that cation-site Ni substitution combined with a high enough doping concentration can decrease the band gap and effectively improve the electronic conductivity in the $Ni_xMn_{3-x}O_4$ crystal structures. Moreover, the highly porous Mn^{4+}-rich structure and amorphous carbon shell lead to fast electron transport and short Zn^{2+} diffusion paths in a mild aqueous electrolyte. On the basis of the above unique structural characterization, the $Ni_xMn_{3-x}O_4$@C ($x = 1$) hybrid displays excellent electrochemical properties with outstanding cycling stability, good rate capability and improved zinc storage performance in comparison to most of the reported cathode materials for ZIBs, with high discharge capacities of 139.7 mA h g^{-1} and 98.5 mA h g^{-1} at 50 and 1200 mA g^{-1} respectively, combined with a nearly 93.5% capacity retention at 400 mA g^{-1} after 800 cycles. These exhibited results indicate that the as-synthesized $Ni_xMn_{3-x}O_4$@C ($x = 1$) would be a prospective candidate as remarkable ZIB cathode materials. Furthermore, this work provides some ideas for not only achieving a good understanding of the intercalation process for divalent metal ions (Zn^{2+}, Mg^{2+}, and Ca^{2+}), but also facilitating the development of aqueous rechargeable alkali ion (K^+, Na^+, and Li^+) and their aqueous rechargeable hybrid batteries.

Conflicts of interest

The authors declare no conflict of interest.

Acknowledgements

This work was financially supported by the National Natural Science Foundation of China (No. 21371180) and the Australian Research Council (ARC) (FT150100109 and DP170102406). The authors acknowledge the Partnership for Advanced Computing, which is supported by the National Science Foundation-Centers of Research Excellence in Science and Technology (NSF-CREST Center) for Innovation, Research and Education in Environmental Nanotechnology (CIRE2N) (Grant No. HRD-1736093). This work has been carried out with the support of the China Scholarship Council (CSC No. 201706370175).

References

1 P. Nayak, E. Erickson, F. Schipper, T. Penki, N. Munichandraiah, P. Adelhelm, H. Sclar, F. Amalraj, B. Markovsky and D. Aurbach, *Adv. Energy Mater.*, 2018, **8**, 1702397.
2 E. Hu, Y. Feng, J. Nai, D. Zhao, Y. Hu and X. Lou, *Energy Environ. Sci.*, 2018, **11**, 872–880.
3 J. Long, Z. Yang, J. Huang and X. Zeng, *J. Power Sources*, 2017, **359**, 111–118.
4 (*a*) Y. Liu, Z. Tai, J. Zhang, W. Pang, Q. Zhang, H. Feng, K. Konstantinov, Z. Guo and H. Liu, *Nat. Commun.*, 2018, **9**, 3645; (*b*) J. Cuan, Y. Zhou, T. Zhou, S. Ling, K. Rui, Z. Guo, H. Liu and X. Yu, *Adv. Mater.*, 2018, **31**, 1803533; (*c*) Q. Zhang, J. Mao, W. Pang, T. Zheng, V. Sencadas, Y. Chen, Y. Liu and Z. Guo, *Adv. Energy Mater.*, 2018, **8**, 1703288.
5 J. Long, Z. Yang, Z. Zhang and J. Huang, *J. Electrochem. Soc.*, 2017, **164**, A3068–A3074.
6 H. Zhang, G. Xia, J. Zhang, D. Sun, Z. Guo and X. Yu, *Adv. Energy Mater.*, 2018, **8**, 1702975.
7 Y. Fang, X. Yu and X. Lou, *Angew. Chem., Int. Ed.*, 2019, **131**, 1–6.
8 S. Wang, Y. Fang, X. Wang and X. Lou, *Angew. Chem., Int. Ed.*, 2019, **131**, 770–773.
9 C. Guan, X. Liu, W. Ren, X. Li, C. Cheng and J. Wang, *Adv. Energy Mater.*, 2017, **7**, 1602391.
10 Y. Huang, M. Zhong, F. Shi, X. Liu, Z. Tang, Y. Wang, Y. Huang, H. Hou, X. Xie and C. Zhi, *Angew. Chem., Int. Ed.*, 2017, **56**, 9141–9145.
11 J. Yu, W. Lu, J. Smith, K. Booksh, L. Meng, Y. Huang, Q. Li, J. Byun, Y. Oh, Y. Yan and T. Chou, *Adv. Energy Mater.*, 2017, **7**, 1600976.
12 S. Galliano, F. Bella, G. Piana, G. Giacona, G. Viscardi, C. Gerbaldi, M. Grätzel and C. Barolo, *Sol. Energy*, 2018, **163**, 251–255.
13 H. Schmies, A. Bergmann, J. Drnec, G. Wang, D. Teschner, S. Kühl, D. Sandbeck, S. Cherevko, M. Gocyla, M. Shviro, M. Heggen, V. Ramani, R. Dunin-Borkowski, K. Mayrhofer and P. Strasser, *Adv. Energy Mater.*, 2018, **8**, 1701663.
14 F. Rigodanza, L. Đorđević, F. Arcudi and M. Prato, *Angew. Chem.*, 2018, **130**, 5156–5161.
15 T. Wang, Z. Kou, S. Mu, J. Liu, D. He, I. Amiinu, W. Meng, K. Zhou, Z. Luo, S. Catechumen and F. Verpoort, *Adv. Funct. Mater.*, 2018, **28**, 1705048.
16 V. Vijayalekshmi and D. Khastgir, *Energy*, 2018, **142**, 313–330.
17 Q. Yun, Q. Lu, X. Zhang, C. Tan and H. Zhang, *Angew. Chem., Int. Ed.*, 2018, **57**, 626–646.
18 (*a*) W. Zhang, W. Pang, V. Sencadas and Z. Guo, *Joule*, 2018, **2**, 1534; (*b*) Y. Liu, Z. Tai, T. Zhou, V. Sencadas, J. Zhang, L. Zhang, K. Konstantinov, Z. Guo and H. K. Liu, *Adv. Mater.*, 2017, **29**, 1703028.
19 W. Li, A. Dolocan, P. Oh, H. Celio, S. Park, J. Cho and A. Manthiram, *Nat. Commun.*, 2017, **8**, 14589.
20 J. Xu, J. Ma, Q. Fan, S. Guo and S. Dou, *Adv. Mater.*, 2017, **29**, 1606454.
21 J. Ju, E. Lee, C. Yoon, S. Myung and Y. Sun, *J. Phys. Chem. C*, 2013, **118**, 175–182.
22 H. Kim, J. Hong, K. Park, H. Kim, S. Kim and K. Kang, *Chem. Rev.*, 2014, **114**, 11788–11827.
23 H. Xu, X. Zhu, K. Sun, Y. Liu and X. Xie, *Adv. Mater. Interfaces*, 2015, **2**, 1500239.
24 G. Jin, H. Qiao, H. Xie, H. Wang, K. He, P. Liu, J. Chen, Y. Tang, S. Liu and C. Huang, *Electrochim. Acta*, 2014, **150**, 1–7.
25 J. Tarascon and M. Armand, *Nature*, 2001, **414**, 359.
26 M. Rahman, A. Glushenkov, T. Ramireddy and Y. Chen, *Chem. Commun.*, 2014, **50**, 5057–5060.
27 C. Xu, B. Li, H. Du and F. Kang, *Angew. Chem., Int. Ed.*, 2012, **51**, 933–935.
28 (*a*) Z. Jia, B. Wang and Y. Wang, *Mater. Chem. Phys.*, 2015, **149**, 601–606; (*b*) B. Sambandam, V. Soundharrajan, S. Kim, M. Alfaruqi, J. Jo, S. Kim, V. Mathew, Y. Sun and J. Kim, *J. Mater. Chem. A*, 2018, **6**, 15530–15539; (*c*) B. She, L. Shan, H. Chen and S. Liang, *J. Energy Chem.*, 2019, **37**, 172–175; (*d*) X. Chen, L. Wang, H. Li, F. Cheng and J. Chen, *J. Energy Chem.*, 2019, **38**, 20–25.
29 B. Zhang, Y. Liu, X. Wu, Y. Yang, Z. Chang, Z. Wen and Y. Wu, *Chem. Commun.*, 2014, **50**, 1209–1211.
30 G. Li, Z. Yang, Y. Jiang, C. Jin, W. Huang, X. Ding and Y. Huang, *Nano Energy*, 2016, **25**, 211–217.
31 D. Kundu, S. Vajargah, L. Wan, B. Adams, D. Prendergast and L. Nazar, *Energy Environ. Sci.*, 2018, **11**, 881–892.
32 M. Alfaruqi, V. Mathew, J. Song, S. Kim, S. Islam, D. Pham, J. Jo, S. Kim, J. Baboo, Z. Xiu, K. Lee, Y. Sun and J. Kim, *Chem. Mater.*, 2017, **29**, 1684–1694.
33 W. Liu, J. Hao, C. Xu, J. Mou, L. Dong, F. Jiang, Z. Kang, J. Wu, B. Jiang and F. Kang, *Chem. Commun.*, 2017, **53**, 6872–6874.
34 N. Zhang, F. Cheng, Y. Liu, Q. Zhao, K. Lei, C. Chen, X. Liu and J. Chen, *J. Am. Chem. Soc.*, 2016, **138**, 12894–12901.
35 Z. Liu, G. Pulletikurthi and F. Endres, *ACS Appl. Mater. Interfaces*, 2016, **8**, 12158–12164.
36 L. Zhou, K. Zhang, Z. Hu, Z. Tao, L. Mai, Y. Kang, S. Chou and J. Chen, *Adv. Energy Mater.*, 2018, **8**, 1701415.
37 H. Kim, D. Seo, H. Kim, I. Park, J. Hong, K. Park and K. Kang, *Chem. Mater.*, 2012, **24**, 720–725.

38 K. Jurewicz, E. Frackowiak and F. Beguin, *Fuel Process. Technol.*, 2002, **77**, 415–421.
39 C. Yuan, J. Li, L. Hou, X. Zhang, L. Shen and X. Lou, *Adv. Funct. Mater.*, 2012, **22**, 4592–4597.
40 P. Hall, M. Mirzaeian, S. Fletcher, F. Sillars, A. Rennie, G. Shitta-Bey, G. Wilson, A. Cruden and R. Carter, *Energy Environ. Sci.*, 2010, **3**, 1238–1251.
41 H. Nan, W. Ma, Z. Gu, B. Geng and X. Zhang, *RSC Adv.*, 2015, **5**, 24607–24614.
42 K. Shaikh, S. Warrick, L. Gurung, D. Kwak and J. Bumpus, *Abstracts of Papers of the American Chemical Society*, 2017, p. 253.
43 X. Lu, W. Bian, Y. Li, H. Zhu, Z. Fu and Q. Zhang, *J. Am. Ceram. Soc.*, 2018, **101**, 1646–1654.
44 S. Greenwald, S. Pickart and F. Grannis, *J. Chem. Phys.*, 1954, **22**, 1597–1600.
45 Y. Zhou, S. Sun, J. Song, S. Xi, B. Chen, Y. Du, A. Fisher, F. Cheng, X. Wang, H. Zhang and Z. Xu, *Adv. Mater.*, 2018, **30**, 1802912.
46 J. Töpfer, A. Feltz, D. Gräf, B. Hackl, L. Raupach and P. Weissbrodt, *Phys. Status Solidi A*, 1992, **134**, 405–415.
47 J. Huang, H. Hsu and C. Cheng, *J. Magn. Magn. Mater.*, 2014, **149**, 358–359.
48 H. Jung, S. Lee, D. Lee and K. Kim, *J. Ceram. Process. Res.*, 2016, **17**, 758–762.
49 Y. Lei, X. Lin and H. Liao, *Sep. Purif. Technol.*, 2018, **192**, 220–229.
50 M. Muralidharan, P. Rohini, E. Sunny, K. Dayas and A. Seema, *Ceram. Int.*, 2012, **38**, 6481–6486.
51 C. Pan, R. Nuzzo and A. Gewirth, *Chem. Mater.*, 2017, **29**, 9351–9359.
52 K. Dokko, M. Mohamedi, N. Anzue, T. Itoh and I. Uchida, *J. Mater. Chem.*, 2002, **12**, 3688–3693.
53 J. Li, S. Xiong, Y. Liu, Z. Ju and Y. Qian, *Nano Energy*, 2013, **2**, 1249–1260.
54 M. Peck and M. Langell, *Chem. Mater.*, 2012, **24**, 4483–4490.
55 H. Xia, Y. Wan, F. Yan and L. Lu, *Mater. Chem. Phys.*, 2014, **143**, 720–727.
56 J. Wang and J. Zhang, *J. Mater. Res.*, 2012, **27**, 928–931.
57 R. Kalubarme, H. Jadhav and H. Park, *Electrochim. Acta*, 2013, **87**, 457–465.
58 M. Chigane and M. Ishikawa, *J. Electrochem. Soc.*, 2000, **147**, 2246–2251.